An in Situ Study Using Anomalous Wide-Angle X-ray Scattering and X-ray Absorption Spectroscopy of the Catalytic System ZnAl 2 O 4 Supported on Alumina

5 AUTHORS, INCLUDING:

Renaud Revel
IFP Energies nouvelles
43 PUBLICATIONS   503 CITATIONS

SEE PROFILE

Dominique Bazin
Collège de France
281 PUBLICATIONS   3,154 CITATIONS

SEE PROFILE

An in Situ Study Using Anomalous Wide-Angle X-ray Scattering and X-ray Absorption Spectroscopy of the Catalytic System ZnAl₂O₄ Supported on Alumina

R. Revel,[*,†,‡] **D. Bazin,**[†] **E. Elkaim,**[†] **Y. Kihn,**[§] **and H. Dexpert**[§]

*LURE, Bât. 209D, Centre Universitaire Paris Sud, BP 34, 91898 Orsay Cedex, France, and
CEMES-CNRS, BP 4347, 31055 Toulouse Cedex 04, France*

A combined approach based on X-ray absorption spectroscopy (XAS), X-ray diffraction (XRD), transmission electron microscopy (TEM), and anomalous wide-angle X-ray scattering (AWAXS) has been used to obtain information on the cation distribution, the electronic state of the metal atoms, and the size of metal oxide clusters for a highly dispersed spinel phase, here the supported system $ZnAl_2O_4/Al_2O_3$. Through numerical simulations of the modulations of the X-ray absorption coefficient and ab initio calculations of the differential diffraction intensities, it has been shown that the tetrahedral sites of the spinel normally occupied by zinc atoms are partially filled. A model of the zinc distribution inside the alumina particles is proposed, in which the zinc atoms are mostly located at the surface of the alumina particle with a concentration gradient between the surface and the particle center. In situ studies reveal a significant increase of the cell parameter as well as a dramatic increase of the Debye−Waller factor associated with the vibrations of the zinc−zinc pairs for a spinel-like environment of zinc when such a phase is submitted to gas−solid reactions such as those employed for automotive exhaust control. An explanation of these two effects is given on the basis of the incorporation of a light atom (such as O) coming from the reactive gases into the solid via the defective properties of the $ZnAl_2O_4/Al_2O_3$ spinel surface.

1. Introduction

The decomposition of nitrogen oxides, which are unwanted pollutants in the atmosphere, has been widely studied. In this context, the copper-exchanged zeolite ZSM-5 is considered as a reference material to reach this goal.[1−3] There are many published studies of catalysts, among which we can distinguish different groups such as metallic particles supported on light oxides (alumina or zeolite) or supported metal oxides.

From a study of different oxides (alumina, silica−alumina, titania, and zirconia), Kintachi et al.[4] reported that acidity of the catalysts is one of the main factors that determine catalytic activity. In the case of perovskites, namely $Sr_2Fe_2O_5$ and $Ca_2Fe_2O_5$, Shin et al.[5] have shown that the difference in their activity for NO decomposition can be explained in terms of their crystallographic properties, i.e., ordering or disordering of the oxygen vacancies. Shimokawabe et al.[6] have demonstrated that over catalysts such as SiO_2, ZrO_2, Al_2O_3, MgO, La_2O_3, Nd_2O_3 and CaO, the decomposition of NO_2 proceeds through an adsorption type mechanism.

This paper deals with ternary AB_2O_4 spinel oxides, which have been the subject of several studies. In one of the first publications,[7] the decomposition of NO_2 through the reaction $2NO_2 + 4CO \rightarrow 2N_2 + 4CO_2$ on $CoFe_2O_4$ was examined. The authors showed that, at a temperature of 300 °C, the oxygen adsorbed on the cobalt ferrite surface during reaction can be in the form of neutral oxygen atoms. Leech et al.[8] have studied different solid solutions ($CuCo_2O_4$, $CuMn_2O_4$, $CuFe_2O_4$, ...) and concluded that for various reasons these solids are doubtful candidates for use as automotive catalysts for the oxidation of CO or reduction of NO_x.

On the other hand, the results published by Shangguan et al.[9] in a study of another group of catalysts (ACr_2O_4 with A = Cu, Mg, Co, Mn, $CoMn_2O_4$, and AFe_2O_4 with A = Cu, Co, Ni) indicate that (i) this kind of material catalyzes the simultaneous removal of NO_x and diesel soot to form carbon dioxide, nitrogen, and nitrous oxide and (ii) spinels are more efficient than simple metal oxide compounds. Panayotov et al.[10] have studied the interaction of CO + NO on $CuCo_{3-x}O_4$ catalysts. They underlined that the NO reduction activity, even in oxidizing conditions, is found to increase with increasing copper content, this trend being linked to an accumulation of reduced sites of the surface layers.

It is obvious that our knowledge of the physicochemical mechanisms will be improved if we can relate the catalytic activity to the structural characteristics of the material. Here, we intend to take a first step in this direction and, more precisely, to show that for a spinel material, major information such as the cation distribution, their electronic state and the size of the metal oxide clusters can be obtained through a combination of X-ray absorption spectroscopy (XAS), X-ray diffraction (XRD), transmission electron microscopy (TEM), and anomalous wide-angle X-ray scattering (AWAXS). This kind of mixed experimental approach has been successfully applied to different systems[11−19] but never, to our knowledge, to a supported catalyst placed under reactive conditions. This work is an attempt to move in that direction, although all the real running conditions are not fulfilled. Our experimental constraints do not allow us to reach this regime; the combination of gases we used does not contain all the components needed, as water vapor or the SO_2/SO_3 mixture present in engine exhaust. We try, however, to keep as close as possible to the real situation and we concentrate on the structural description on the material placed under a certain type of reactive conditions. The material selected for this study is a supported catalytic system $ZnAl_2O_4/Al_2O_3$.

[†] Centre Universitaire Paris Sud.
[‡] Present address: Institut Français du Pétrole, 1-4 Avenue de Bois-Préau, 92852 Rueil-Malmaison Cedex, France. Tel: 33 1 47 52 57 42. Fax: 33 1 47 52 60 55. E-mail: renaud.revel@ifp.fr.
[§] CEMES-CNRS.

TABLE 1: Structural Parameters Obtained for the Reference Compound ZnAl$_2$O$_4$ through a Numerical Simulation of the Experimental Diagrams Taken at 9200 and 9661.5 eV Using the Rietveld Method

λ (Å)/E (eV)	1.34766/9200	1.28329/9661.5		
step (2θ, deg)	0.05	0.05		
angular range (2θ, deg)	15−130	15−122		
no. of diffraction peaks	47	48		
Rp	9.13	15.8		
R_wp	10.3	10.1		
χ^2	3.7	1.4		
R_{Bragg}	5.69	5.28		
R_F	5.26	6.24		
$f\,'(e^-)$	−2.92	−8.51		
$f\,''(e^-)$	0.53	1.3		
cell parameters (Å)	$a = b = c = 8.0823(3)$	$a = b = c = 8.0821(4)$		
atoms	$x = y = z$	B_{iso} (Å)	$x = y = z$	B_{iso} (Å)
Zn^{2+}	0.125	0.70(2)	0.125	0.79(4)
Al^{3+}	0.5	0.3	0.5	0.3
O^{2-}	0.2640(1)	0.6	0.2633(2)	0.6

TABLE 2: Best Fit Results of the EXAFS Oscillations for the Spinel ZnAl$_2$O$_4$ Model Compound and the Catalyst ZnAl$_2$O$_4$/Al$_2$O$_3$

		ZnAl$_2$O$_4$			ZnAl$_2$O$_4$/Al$_2$O$_3$		
		d (Å)					
paths	N^a	XRD	EXAFS	σ^2 (Å^2)	N	d (Å)	σ^2 (Å^2)^b
Zn−O−Zn	4	1.956	1.947 ± 0.005	0.0036 ± 0.0008	4.0 ± 0.5	1.954 ± 0.003	0.004 ± 0.002
Zn−Al−Zn	12	3.352	3.35 ± 0.01	0.005 ± 0.001	10.9 ± 0.9	3.355 ± 0.004	0.005 ± 0.002
Zn−O−Zn	12	3.394	3.40 ± 0.02	0.011 ± 0.001	10.9 ± 0.9	3.41 ± 0.02	0.011 ± 0.002
Zn−Zn−Zn	4	3.501	3.50 ± 0.01	0.009 ± 0.001	0.9 ± 1	3.50 ± 0.01	0.009 ± 0.002
Zn−Al−O−Zn	24	3.609	3.62 ± 0.02	0.003 ± 0.002	23 ± 3	3.63 ± 0.01	0.003 ± 0.002
Zn−O−Zn	12	4.272	4.27 ± 0.03	0.002 ± 0.002	6.6 ± 3	4.26 ± 0.02	0.002 ± 0.002
Zn−Al−O−Zn	24	4.375	4.36 ± 0.03	0.003 ± 0.002	14.3 ± 3	4.34 ± 0.03	0.003 ± 0.002
χ^2_ν			1.6			1.4	
R_f			0.009			0.011	

^{a} Fixed for the fit. ^{b} A general σ^2 was refined and added to the σ^2 values obtained with the fit of the ZnAl$_2$O$_4$ model compound for each path.

For the interpretation of EXAFS data, numerical simulation of the modulations of the absorption coefficient taking into account multiple scattering processes have been performed. Moreover, diffraction diagrams being dominated by the contribution of the alumina support, the usual analysis based on the Rietveld method has to be replaced by ab initio calculations of the differential scattering intensities based on the Debye equation.

2. Experimental Section

Sample Preparation. The supported catalytic system ZnAl$_2$O$_4$/γ_c-Al$_2$O$_3$ (atomic composition: 2.3% of Zn, 38.1% of Al, and 59.6% of O) was prepared from Zn(NO$_3$)$_2$·6H$_2$O and alumina SB3 from Condea by atomization. The compound was then calcined under air at 750 °C for 2 h. Its BET total surface area, determined with nitrogen adsorption at 77 K, is 131 m^2/g.

X-ray Diffractometry. Standard X-ray powder patterns were recorded on a vertical X-ray diffractometer (Philips PW 1800), using Cu Kα radiation generated at 40 keV and 40 mA, which is equipped with automatic variable slits, a diffracted beam graphite monochromator, a proportional counter, and a pulse height analyzer. A typical scan speed of 0.02° 2θ/s was used.

Diffraction experiments were carried out using the synchrotron radiation on the DCI storage ring at LURE. The experiments were performed on the W22 wiggler beamline equipped with a Si (111) double crystal monochromator. The energy calibration was made by recording the fluorescence of the sample for comparison with XAS measurements done in transmission mode. To limit the variation of the absorption coefficient, the anomalous diffraction experiments were performed at 7.5 and 400 eV below the zinc K edge. The diffraction diagrams were recorded in θ/2θ step scan mode in the range 0.5 Å^{-1} < k < 8.5 Å^{-1}. The incident beam was limited by an entrance slit of 2 mm × 4 mm and monitored by an ionization detector. The

scattered beam was collected through Sollers slits giving a 0.08° (2θ) angular resolution (negligible compared to the width of the catalyst peaks) in a NaI scintillation detector. Differential intensities are obtained after correcting the experimental spectra for fluorescence, inelastic scattering, geometry, and high k proportional normalization.

Electron Microscopy. The electron microscope used was a Philips CM20T equipped with a Tracor energy-dispersive X-ray spectrometer (EDXS) and a Gatan 666 device for parallel electron energy loss spectroscopy (PEELS). The microscope was operated in the bright field imaging mode, selected area diffraction mode (SAD), and PEELS analysis mode (diffraction coupled). The sample powder was dispersed, after grinding on a microgrid with a holey carbon film as support. The spot sizes used for EELS analysis were 60 and 15 nm.

EXAFS Spectrometer. The catalysts were in powder form, sieved to 100−200 μm, and XAS spectra were recorded by pouring an appropriate quantity of the sample in a thin graphite frame. Full details on the different equipment used in this study can be found in ref 20. The absorber thickness of the different samples was chosen such that $\mu x = 1$ (μ is the linear absorption coefficient) and care was taken in order to make the samples of uniform thickness.

The XAS spectra were performed at LURE on the D44 station of the DCI storage ring running at 1.85 GeV with an average current of 300 mA and a lifetime of 200 h. The X-rays were monochromatized by two Si (311) single crystals and the incident I_0 and transmitted I_1 intensities were recorded by use of two ionization chambers filled with argon. This monochromator, operating with 1 mm vertical slits, has an energy resolution of 2.3 eV at 10 keV. Calibration of the experiment was made with a reference zinc metal foil. Data treatment was carried out using EXAFSPOWER code.[21] The preedge region
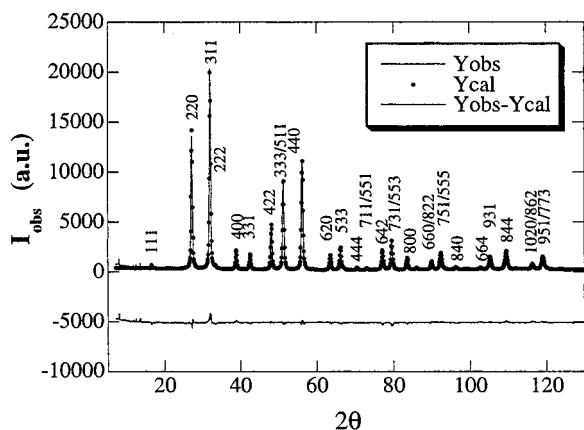
Figure 1. Experimental diffraction intensity of the model compound ZnAl₂O₄ taken at 9200 eV (Y_{obs}) compared to calculated diffraction intensity (Y_{cal}).
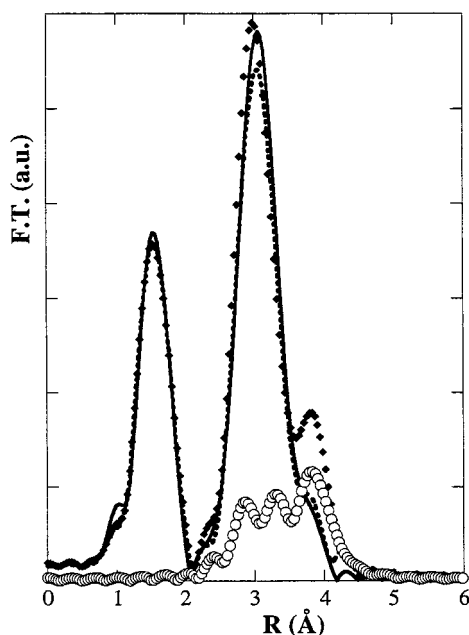
Figure 2. Modulus of the FT of the experimental data of the ZnAl₂O₄ spinel (line) compared to the numerical simulation (dashes) including single (diamonds) and multiple scattering contributions (circles).

was removed by using a linear function. Atomic absorption was modeled by using a 5th degree polynomial. Following Lengeler-Eisenberger normalization, EXAFS oscillations were Fourier transformed (FT) using a Kaiser window ($\tau = 2.5$) between 3.5 and 12.6 Å^{-1}. Filtering EXAFS spectrum was obtained by back Fourier transformation between 0.86 and 3.93 Å. Errors were estimated after determination of the data mean standard deviation in $\chi(k)$ using the STATEXAFS[22] code.

For the chemical treatment, the catalysts were placed in a furnace[23] under a flow of 330 ppmv NO/330 ppmv C₃H₆/370 ppmv CO/11% O₂/11% CO₂/balance N₂ for a NHSV (Normal Hourly Space Velocity) of 5000 h^{-1}. The temperature of the sample was then increased to 500 °C. The EXAFS spectra were recorded at different temperatures (30 °C, 300 °C, 400 °C, 500 °C, 30 °C) after an equilibration time of 30 min at each temperature. The typical acquisition time for an EXAFS spectrum was 15 min and three spectra were taken for all the temperatures. A similar experiment was performed without reactive gas (in air) in order to distinguish between the effects of the two parameters (gas and temperature).
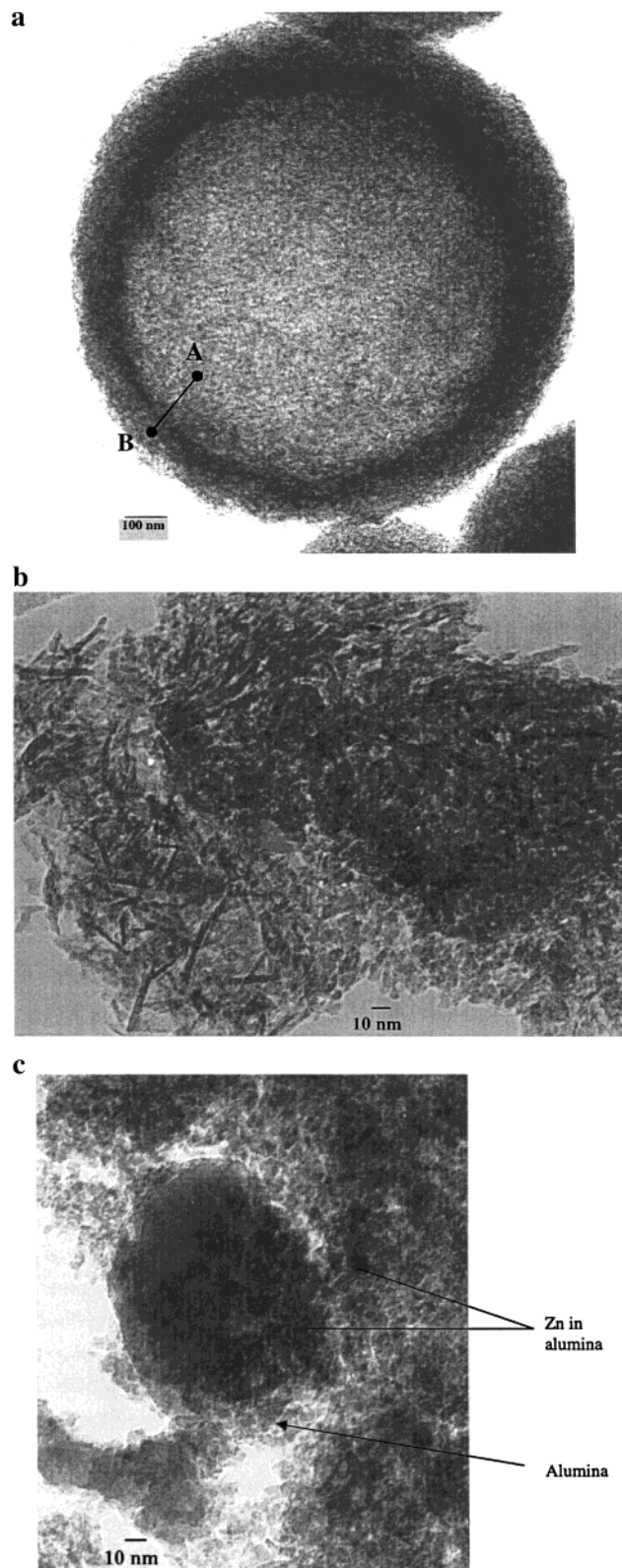
Figure 3. TEM images of ZnAl₂O₄/Al₂O₃: (a) general view of a grain of the catalyst; (b) A zone containing Zn; (c) B zone.

3. Theoretical Background

Anomalous Wide-Angle X-ray Scattering (AWAXS). In AWAXS, use is made of the energy dependence of the atomic scattering factor, $f(k,E)$, near an absorption edge. This parameter is expressed in electron units as

$$f(k,E) = f_0(k) + f'(k,E) + if''(k,E) \qquad (1)$$

In Situ Study of the Catalytic System ZnAl$_2$O$_4$/Alumina

J. Phys. Chem. B, Vol. 104, No. 42, 2000 **9831**

where $\vec{k}$ ($k = 4\pi \sin \theta/\lambda$) bisects the angle between the incident and scattered directions and also defines the scattering plane. $f(k,E)$ denotes the amplitude of the radiation coherently scattered by a single atom and is composed of an energy independent part, $f_0(k)$, and a real and imaginary energy dependent correction, $f'(E)$ and $f''(E)$. Assuming a random (powder) arrangement of the structure with respect to the incoming X-ray beam, for a multiatom system, the intensity of coherently scattered X-rays[24] is given by

$$I(k,E) = \Sigma_i \Sigma_j f_i(k,E) f_j(k,E) \sin(kR_{ij})/kR_{ij} \qquad (2)$$

In this equation, $I(k,E)$ is the intensity from coherent scattering, the sums over i and j are over all the atoms, R_{ij} being the distance between the atom i and j and f_i and f_j being the atomic scattering factors. The success of the AWAXS technique depends on accurate determination of the atomic scattering factors. For the classical part, $f_0(k)$, we use the Cromer and Mann parameters.[25] The determination of the dispersive factor f'' was carried out using the photoelectronic cross section μ and the optical theorem. The evaluation of f' was made using the Kramers−Kronig relationship. Details on the evaluation of the dispersive factors can be found elsewhere.[14−15]

Figure 1 shows the diffraction intensity of the model compound ZnAl$_2$O$_4$ obtained on the wiggler beam line, the energy of the photon being 9200 eV. The experimental diagram was simulated using the Rietveld method (program FULL-PROF[26]) and the different structural parameters obtained are gathered in Table 1. A similar approach has been used for the diffraction diagram collected at 96 61.5 eV (Table 1).

Most of the discussion regarding the diffraction technique will thus be on the differential intensities. Basically, we proceed to an accurate comparison between the experimental signals and the numerical simulation using the Build program,[16,17] which has been linked to the Cerius package.[27]

X-ray Absorption Spectroscopy. The analytical procedure of the experimental EXAFS data using calculated curved-wave and multiple scattering as described by Rehr et al.[28,29] has been used. They express the EXAFS spectrum as a sum of different multiple scattering contributions, and each such contribution can be written in the form

$$\chi_n(k) = \chi_0{}^n(k) \exp(-L_n/L_n - 2k^2\sigma^2) \qquad (3)$$

and

$$\chi_0{}^n(k) = F_n(k) \sin(kL_n + \theta_n(k)) \qquad (4)$$

where n represents different single or multiple scattering paths, L_n is the total path length, and λ_n is the mean free path associated with each path. $F_n(k)$ and $\theta_n(k)$ are the amplitude and phase of the backscattered wave that depend on k, on the scattering path involved, and on the atomic potential parameter. The authors have shown in this paper that above the first shell, multiple scattering contributions cannot be systematically neglected and may in certain cases even be dominant.

Simulation of EXAFS spectra was carried out using FeFF7.02 code.[30] The FeFF parameters were the following: maximum number of scattering legs = 5, maximum scattering length = 5 Å, exchange correlation potential = Hedin − Lundqvist, energy threshold shift = −5 eV, inelastic losses $S_0{}^2 = 1$, plane wave filter = 1.2%, curved wave filter = 1.7%. The FT of the experimental data of the ZnAl$_2$O$_4$ spinel reference material is compared in Figure 2 with the numerical simulation (total) including various multiple scattering contributions (single and

multiple scattering) in order to show the quality of the numerical simulation of the experimental data. As expected,[31] if only single scattering contributions are important for the first shell, this is definitely not the case for the higher shells. Notice that double scattering contributions are much larger than the contribution from single scattering alone.

The refinement was performed using FEFFIT code.[32] First, to validate the fitting procedure, the filtered EXAFS spectrum of the ZnAl$_2$O$_4$ reference compound with (i) the phases $\Phi(\pi, k, R)$, amplitudes $f(\pi, k, R)$ amplitudes, electron mean free path and inelastic losses $S_0{}^2$ extracted from the FeFF simulation of ZnAl$_2$O$_4$ and (ii) the 7 single and multiple scattering paths extracted from the above simulation was refined. Fitting parameters were set as follows: energy threshold E_0 was fixed to 0 eV (the choice of E_0 was made in the FeFF simulation taking the energy threshold shift equal to −5 eV), coordination numbers N of all the paths were fixed to their crystallographic values, Debye−Waller factors σ^2 and distances R of each path were allowed to vary. Thus, 14 variables have been used during the fit for 18 independent parameters ($N_{idp} = 2\Delta k\Delta R/\pi +1$). The goodness of fit was expressed by the $\chi^2{}_\nu$ and R_f factor.[33] Table 2 shows the parameters−coordination number N, interatomic distance R, and Debye−Waller factor σ^2—that were respectively used and obtained in the fitting procedure.

For the catalyst, the starting conditions for the fitting routine were taken to be equal to the result of the above fit. The experimental EXAFS modulations are fitted using a general Debye−Waller factor, the distances and the coordination numbers associated with the 7 paths. Thus, 15 variables have been used during the fit for 18 independent parameters. The E_0 energy shift parameter was not refined due to its very important correlation with the distance R.

For the in situ experiments, the fitting starting conditions were taken equal to the result of the respective ex-situ fits (ZnAl$_2$O$_4$ model compound or catalyst). At first, analysis of the first shell (4 Zn−O at 1.95 Å) was performed on the in situ experiments (in air and in reactive gas flow for the reference material ZnAl$_2$O$_4$ and the catalyst). No variation of the coordination number (distance variation or substitution of oxygen by C, O, or N) was found. At second, analysis of the filtered EXAFS spectra, obtained by back Fourier transformation of data between 0.86 and 3.93 Å, was made. The Debye−Waller factor (σ^2) of each path was refined and the coordination number (N) of each path was fixed to the value previously determined in the ex-situ fit. The distance parameters were lumped together into a unique cell parameter a (cubic cell) and all the fits were based on an isotropic dilatation.

4. Ex Situ Results Obtained on the ZnAl$_2$O$_4$/Al$_2$O$_3$ Catalyst

Electron Microscopy. Electron microscopy shows that the specimen is dominated by spherical grains, the size of which is 1−3 μm in diameter. Each spherical grain is an agglomerate of smaller particles with two morphologies, as shown by the conventional TEM image of the cross section of a grain (Figure 3a). In the center, needle-shaped crystals can be related to the γ-Al$_2$O$_3$ phase (Figure 3b). EELS analysis reveals that no Zn is detected in the needles, so these needle-shaped particles can be considered as pure alumina. The second type of particles has the form of little spheres of approximately 5 nm in diameter (Figure 3c). EELS analysis made on these small spheres gives Zn, Al, and O with different zinc concentrations. The probe size is too large compared to the particle size to determine the distribution of the different elements of the individual catalyst particles. By using a 10 nm probe, a profile of the Zn concen-
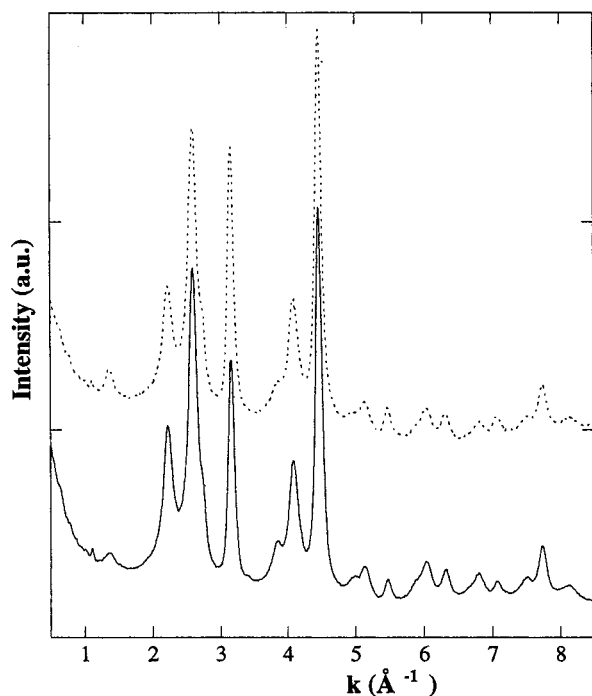
Figure 4. Diffraction patterns for the $ZnAl_2O_4/Al_2O_3$ catalyst collected at 9200 eV (line) and 9661.5 eV (dashes).
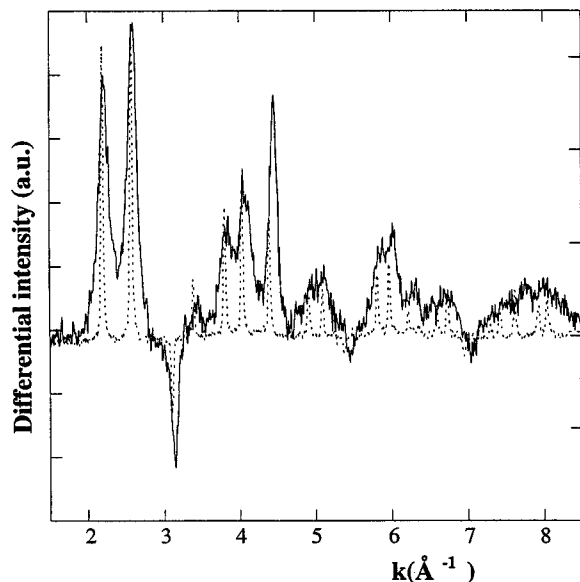
**Figure 5.** Difference in scattered intensities of the catalyst $ZnAl_2O_4/Al_2O_3$ (line) compared to an the difference in scattered intensities of the reference compounds $ZnAl_2O_4$ (dashed).

tration, from the position marked (A) to the position (B) in Figure 3a, was obtained. The profile shows an increase in Zn content from (A) where $Zn/O = 0$ to the darker part of the crown (maximal atomic ratio $Zn/O = 0.07$) and then a decrease up to (B) where $Zn/O = 0.02$. This Zn concentration profile confirms that the Zn is included in the small spherical particles of the crown. The decrease of the Zn content in the outermost part of the grains is in agreement with the presence of some needle-shaped particles mixed with the spheres at the surface of the grains, as revealed by the TEM pictures.

X-ray Diffraction. Figure 4 shows the diffraction patterns at each of the two energies we considered here, namely 9200 and 9661.5 eV. In Figure 5, the difference in scattered intensities of the catalyst has been compared with the differential intensity
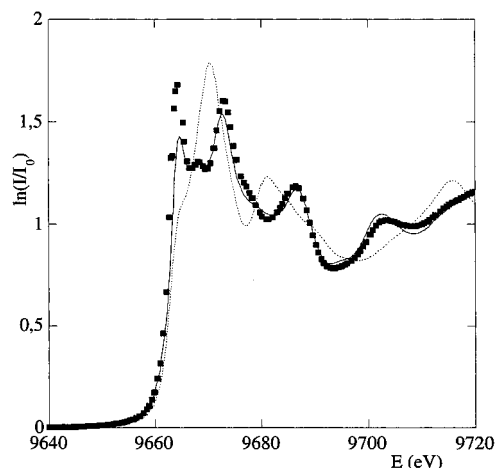
Figure 6. Near edge region at the zinc K edge of the catalyst (square), ZnO (dashes), and $ZnAl_2O_4$ (line).
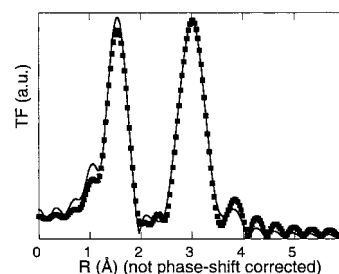
Figure 7. Moduli of the FTs of the EXAFS modulations collected at room temperature for the catalyst (line) and its best fit (square).

of the model compound $ZnAl_2O_4$. It is seen that the distribution of zinc atoms in the catalyst is spinel like with a significant contraction of the cell (the peaks are shifted to higher values of k).

XANES Spectra. The near edge region of the two model compounds ($ZnAl_2O_4$ and ZnO) and the catalyst are compared in Figure 6. The energy of the catalyst edge (9664.5 eV) clearly establishes that the electronic state of the zinc atom is 2+ (9664.8 eV for ZnO, 9664.6 eV for $ZnAl_2O_4$, and 9659 eV for Zn metal). The structural features between the catalyst and the $ZnAl_2O_4$ spinel above the edge are very similar.

EXAFS Spectra. The FT of the EXAFS modulations (experimental and calculated spectra) taken at room temperature are shown in Figure 7. The result of the fit, corresponding to the best reduced ($\chi^2_\nu = 1.4$), is summarized in Table 2. The original sample presents an average zinc—oxygen coordination number of 4.0 in line with a tetrahedral coordination. The different coordination numbers as well as the interatomic distances associated with the second shell confirm the fact that the distribution of zinc atoms is spinel-like and indicate a significant loss of Zn^{2+} cations inside the network.

5. In Situ EXAFS Results Obtained on the $ZnAl_2O_4/Al_2O_3$ Catalyst

XANES Spectra. The different near-edge spectra have not been plotted because neither the shape nor the position changes with the temperature or with the gas environment. Thus, the electronic state as well as the nature of the coordination polyhedra of the zinc atom remain the same.

EXAFS Spectra. The moduli of the FT of the EXAFS spectra collected at different temperatures in air (30 °C, 300 °C, 400 °C and 500 °C) are plotted on Figure 8, which shows that the shape of the modulus changes with the temperature. The different coordination numbers and the interatomic distances
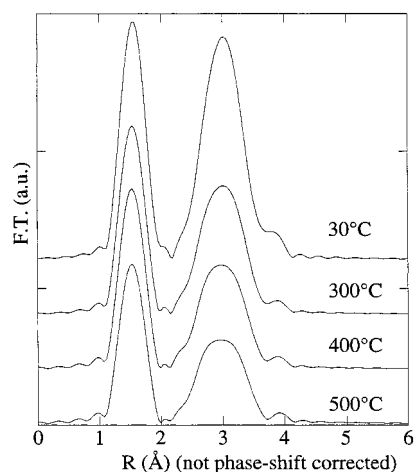
Figure 8. Moduli of the FTs collected at different temperatures during the first set of experiments performed on the catalyst.

of the first shell (number of oxygen atoms around zinc atoms) and the second shell (number of oxygen atoms, aluminum atoms, and zinc atoms around zinc atoms), obtained by fitting the data, are given in Table 3. In this case, the numerical refinements were based on an isotropic dilatation because the cell is cubic. Thus, all the distances were functions of the cell parameter a. The different numerical simulations indicate that for a temperature between 30 and 500 °C, there is no change in Zn coordination number when the sample is heated. In fact, since all these structural parameters retain their values, the modifications of the FT can be linked to an increase of the Debye–Waller factor with the temperature.

For the second experiment (with reactive gas flow), the moduli of the FTs are plotted in Figure 9 and the structural parameters obtained from the numerical simulation of the EXAFS modulations are listed in Table 4. It is clear that a significant variation of the Debye–Waller factor and the cell parameter is measured. As shown in Figure 10, a significant increase of this Debye–Waller factor is measured when the catalyst is in reactive gas flow when compared with the results obtained in the experiment without the reactive gases. The conclusion is the same when comparison is made with the results obtained on the reference compound (ZnAl₂O₄) in reactive gas flow.
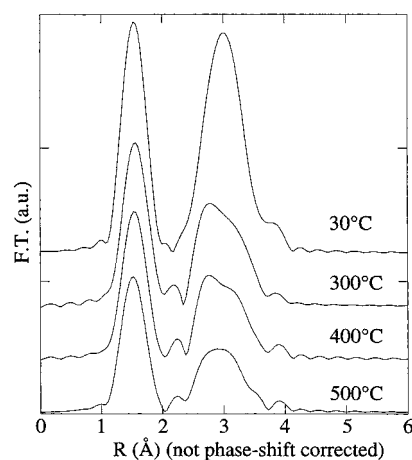
Figure 9. Moduli of the FTs collected at different temperatures during the second set of experiments performed on the catalyst.
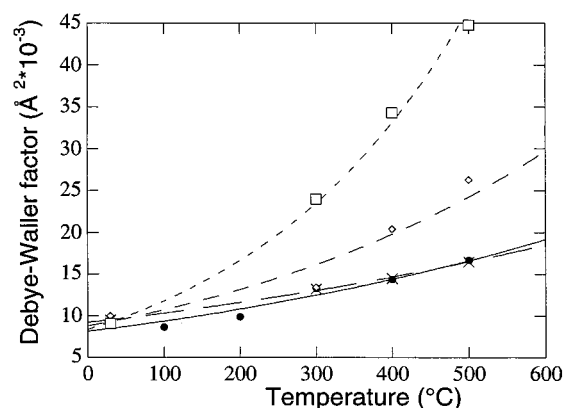
Figure 10. Debye–Waller factor versus the temperature for the reference compound in air (dots) and in the reactive gases (cross) and for the catalyst in air (diamond) and in the reactive gases (square).

6. Discussion

Electron microscopy observations form the starting point of the discussion by indicating that the distribution of the zinc atoms in the solid catalyst is inhomogeneous on the level of the grain of 1–3 μm in size. These grains are composed of particles of two morphologies, needle-shaped and spherical, which again are associated with pure alumina and zinc–alumina particles, respectively. Anomalous scattering experiments and

TABLE 3: Best Fit Results of the EXAFS Oscillations for the Catalyst ZnAl₂O₄/Al₂O₃ for the First Experiment (without Gas or in Air)

T (°C)	Zn–O–Zn ($N = 4$)[a] σ^2 (Å²)	Zn–Al–Zn ($N = 10.9$)[a] σ^2 (Å²)	Zn–O–Zn ($N = 10.9$)[a] σ^2 (Å²)	Zn–Zn–Zn ($N = 0.9$)[a] σ^2 (Å²)	Zn–Al–O–Zn ($N = 23$)[a] σ^2 (Å²)	Zn–O–Zn ($N = 6.6$)[a] σ^2 (Å²)	Zn–Al–O–Zn ($N = 14.3$)[a] σ^2 (Å²)	a (Å)	χ^2_ν	R_f
30	0.004 ± 0.002	0.005 ± 0.002	0.011 ± 0.002	0.009 ± 0.002	0.003 ± 0.002	0.002 ± 0.002	0.003 ± 0.002	8.080	1.4	0.011
300	0.005 ± 0.002	0.009 ± 0.003	0.016 ± 0.003	0.013 ± 0.003	0.005 ± 0.003	0.005 ± 0.003	0.004 ± 0.003	8.085	1.5	0.013
400	0.005 ± 0.002	0.010 ± 0.002	0.019 ± 0.002	0.020 ± 0.002	0.006 ± 0.002	0.006 ± 0.002	0.005 ± 0.002	8.086	1.4	0.010
500	0.006 ± 0.002	0.011 ± 0.002	0.021 ± 0.002	0.026 ± 0.003	0.007 ± 0.002	0.007 ± 0.002	0.006 ± 0.002	8.089	1.4	0.010
30	0.003 ± 0.002	0.005 ± 0.003	0.012 ± 0.003	0.010 ± 0.003	0.002 ± 0.003	0.002 ± 0.003	0.002 ± 0.003	8.085	1.4	0.012

[a] Fixed for the fit.

TABLE 4: Best Fit Results of the EXAFS Oscillations for the Catalyst ZnAl₂O₄/Al₂O₃ for the Second Experiment (with Reactive Gases)

| T (°C)	Zn–O–Zn ($N = 4$)[a] σ^2 (Å²)	Zn–Al–Zn ($N = 10.9$)[a] σ^2 (Å²)	Zn–O–Zn ($N = 10.9$)[a] σ^2 (Å²)	Zn–Zn–Zn ($N = 0.9$)[a] σ^2 (Å²)	Zn–Al–O–Zn ($N = 23$)[a] σ^2 (Å²)	Zn–O–Zn ($N = 6.6$)[a] σ^2 (Å²)	Zn–Al–O–Zn ($N = 14.3$)[a] σ^2 (Å²)	a (Å)	χ^2_ν	R_f
30	0.003 ± 0.002	0.005 ± 0.002	0.011 ± 0.002	0.009 ± 0.002	0.002 ± 0.002	0.001 ± 0.002	0.003 ± 0.002	8.084	1.5	0.012
300	0.005 ± 0.002	0.009 ± 0.003	0.018 ± 0.004	0.024 ± 0.004	0.005 ± 0.004	0.005 ± 0.004	0.004 ± 0.004	8.092	1.8	0.03
400	0.006 ± 0.002	0.011 ± 0.002	0.020 ± 0.003	0.034 ± 0.003	0.06 ± 0.003	0.07 ± 0.002	0.06 ± 0.003	8.101	1.7	0.022
500	0.007 ± 0.002	0.014 ± 0.002	0.024 ± 0.002	0.045 ± 0.003	0.09 ± 0.002	0.010 ± 0.002	0.008 ± 0.002	8.110	1.6	0.015
30	0.003 ± 0.002	0.005 ± 0.002	0.011 ± 0.003	0.010 ± 0.003	0.002 ± 0.002	0.002 ± 0.002	0.003 ± 0.002	8.086	1.5	0.014
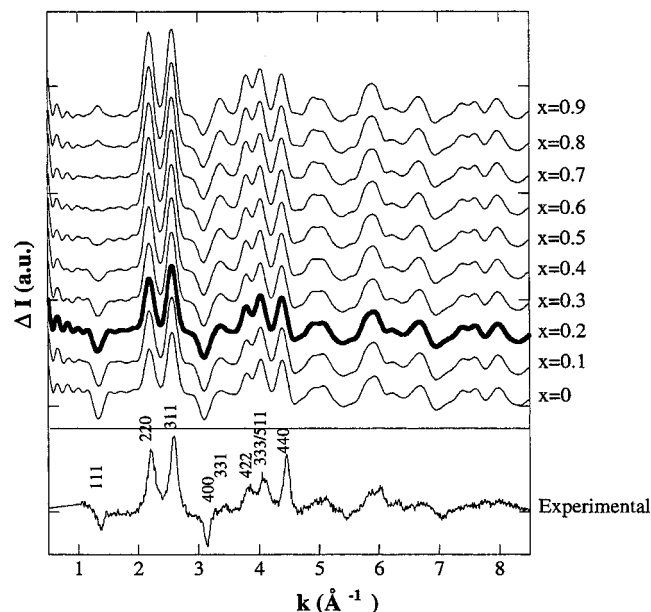
Figure 11. Numerical simulations based on a substitution Al/Zn of $(Zn_{1-x}Al_x)_{Td}(Al_2)_{Oh}O_4$ with $x = 0-0.9$.

XAS investigations give information about the local order around zinc atoms inside the zinc−alumina particles only. As shown in Figure 6, the local structure around zinc atoms can be considered to be similar to that existing for a $ZnAl_2O_4$ spinel. The first numerical simulations (Build program) were done in order to estimate the coherence length associated with such $ZnAl_2O_4$ entities, and it seems that this parameter is around 40 Å, i.e., the smallest particles viewed by electron microscopy. Nevertheless, some structures, such as the (111) feature as well as the intensity ratio between the (220) and the (311) features are not properly taken into account. Thus, a second set of numerical simulations based on a Al/Zn substitution starting from the $(Zn_{1-x}Al_x)_{Td}(Al_2)_{Oh}O_4$ composition with $x = 0-0.9$ were performed. These calculations lead to the differential intensities plotted in Figure 11. The experimental results can be accurately reproduced for $x = 0.2$, especially the features at (111), (220), and (311).

We have to consider now the results given by the XAS measurements. The best fit indicates that the number of zinc−zinc bonds at 3.50 Å is 1 in the catalyst but 4 in the $ZnAl_2O_4$ model compound. To balance this cation lack, we tried to introduce aluminum atoms in place of zinc in the fitting procedure. The best simulation corresponds to 0.4 zinc−aluminum distances at 3.50 Å but does not significantly improve the quality of the fit ($\chi^2_\nu = 1.35$), confirmed by the F test.[34] This confirms that the tetrahedral sites of the spinel close to the site occupied by zinc atoms have a significant partial occupation. Furthermore, simulation (in terms of number of interatomic distances) of the EXAFS spectra (Table 5), taking into account the cluster sizes, shows that a spinel-type formulation cannot describe correctly these EXAFS results, especially the number of zinc−zinc distances. Thus, in the present case, for which the coherence length is around 40 Å, it appears that there is only one zinc−zinc distance at 3.50 Å instead of the three in $ZnAl_2O_4$ clusters of similar size.

To understand the distribution of the zinc atoms in the cluster, we performed three further simulations. Introducing vacancies in $ZnAl_2O_4$ clusters leads to a third occupation of the 8 tetrahedral sites, which are fully occupied in a normal spinel ($\tau = 0.33$), but with a different zinc distribution inside the clusters (either homogeneous distribution, Zn at the surface, or
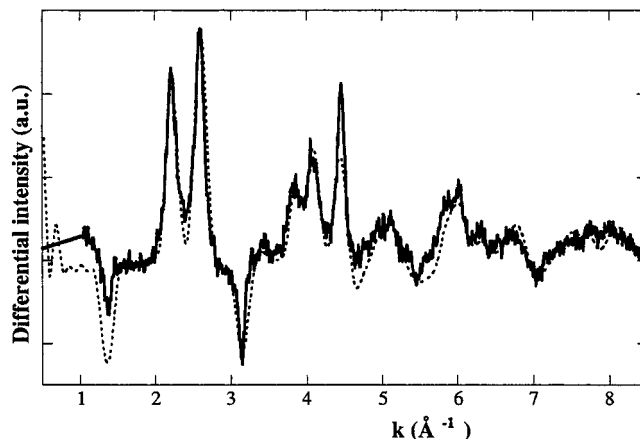
Figure 12. Differential calculated at the zinc K edge for some selected clusters.

TABLE 5: Variation of the Number of Neighbors with the Cluster Size and the Zinc Vacancies

size (Å)	$N(Zn-Al)$ @ 3.35 Å	$N(Zn-O)$ @ 3.38 Å	$N(Zn-Zn)$ @ 3.50 Å
	Simulated Clusters		
20	7.9	7.5	2.3
30	10.1	9.7	2.7
40	10.0	10.2	3.0
50	10.2	10.2	3.2
60	10.6	10.5	3.4
70	10.8	10.8	3.5
77.25	10.9	10.9	3.5
	Experimental Cluster		
40	10.9	10.9	1
	Cluster with Homogeneous Vacancies		
40	9.7	9.8	1.3
	Cluster with zinc at the Surface		
40	8.7	9.0	1.9
	Cluster with Zinc at the Center		
40	11.5	11.5	2.7

Zn at the center). The results (Table 5) show that the quantity of zinc could be homogeneously defective or at the surface in the total cluster.

To integrate this XAS result in the ab initio diffraction calculations performed on the differential intensity, a third set of calculations was done on the basis of this lack of zinc atoms inside the network. We consider now only $ZnAl_2O_4$ clusters for which the number of cations and anions respect the electroneutrality of the entities. The best result, obtained for a cluster with the $Zn_{0.5}Al_{1.88}O_{3.32}$ formula, is compared to the catalyst differential spectrum in Figure 12. This result corresponds to $\tau = 0.33$, previously determined. Owing to uncertainties of the EXAFS technique concerning the number of neighbors and the incomplete agreement of the diffraction on the (111) feature, we can consider that the coordination numbers given by these two techniques are in agreement.

However, the cell parameter deduced form EXAFS is 8.08 Å whereas the one obtained from AWAXS is 7.98 Å. Considering that the error on these values is low ($\Delta a = 0.03$ Å for these two techniques for this compound), this difference is significant and astonishing.

To explain these apparently conflicting results, we propose a model detailing the zinc distribution inside the spherical clusters (Figure 13). This model ("spheroid"), assumes that the zinc cations diffused in the alumina structure during the synthesis. The diffusion occurs via the tetrahedral sites because of the tetrahedral preference of the Zn^{2+} cation.[35,36] This introduction of zinc is accompanied by the migration of

In Situ Study of the Catalytic System ZnAl₂O₄/Alumina

J. Phys. Chem. B, Vol. 104, No. 42, 2000 **9835**

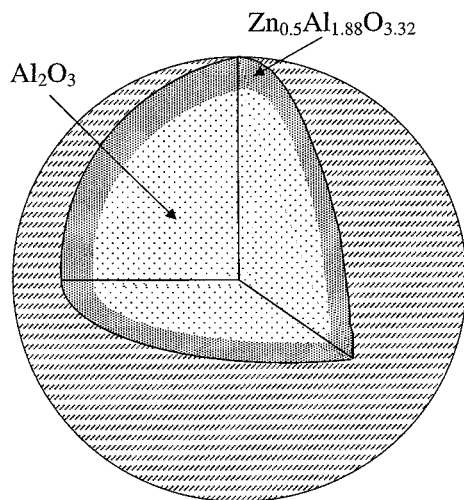Al_2O_3

$Zn_{0.5}Al_{1.88}O_{3.32}$

Figure 13. "Spheroid" model.

aluminum atoms toward octahedral sites and by the appearance of oxygen vacancies (to respect the local electroneutrality). This transformation of the alumina structure into the $ZnAl_2O_4$ type structure can also explain the local cell dilatation. Thus, our model consists of spherical clusters with a progressively decreasing quantity of zinc from the surface to the center. In this description, there is obviously a cell parameter gradient between the center (mostly alumina, cell parameter $a = 7.94$ Å) and the surface ($ZnAl_2O_4$ structure with vacancies, $a = 8.08$ Å). This model can explain the discrepancy between EXAFS, which is mostly sensitive to the zinc rich regions, and diffraction, which gives an average cell parameter.

Regarding the in situ experiments, key information on the structural behavior of the solids versus the reactive gases is obtained. For the first set of experiments, a familiar effect of temperature is measured with a simple increase of the Debye−Waller factors associated with each kind of neighbor around the zinc atoms. At the opposite extreme, if a flow of reactive gases is passed through the sample, a dramatic increase of the Debye−Waller factor related to the zinc−zinc pairs is observed as well as an expansion of the cell parameter. A possible explanation of these two effects can be given by the inclusion of a light atom in the host structure; i.e., the light element coming from the reactive gases (such as oxygen) diffuses into the solid. This element could not be detected with the EXAFS parameter N because (i) its great similitude with the first shell of oxygen around the Zn atom regarding the atomic number Z and (ii) the uncertainty in the number N.

7. Conclusion

It has been shown in this work that a combined approach of AWAXS and EXAFS techniques leads to information on local and medium range order around zinc atoms on well-dispersed phases. We also mention that this combination completes the limited information obtained with the usual (in lab) characterization techniques such as electron microscopy or X-ray diffraction. The compound $ZnAl_2O_4/Al_2O_3$, present as small clusters (40 Å) in which the zinc distribution is not homogeneous, reveals in fact a defective spinel structure in Zn^{2+} and O^{2-} around the zinc atoms. This observation is consistent with the decrease of the cell parameters toward ideal $ZnAl_2O_4$ structure.

Moreover, for in situ EXAFS studies, we have shown, in the presence of reactive gases, an expansion of the cell parameters and a dramatic increase of the Debye−Waller factor of Zn−Zn pairs with temperature. A possible explanation of this behavior is the inclusion of light atoms coming from reactive gases.

Finally, these different experimental results obtained from structural investigations as well as the ab initio calculations demonstrate the types of complementary information that can be obtained by using different techniques for characterization of highly disordered and reactive solids.

References and Notes

(1) Iwamoto, M.; Mizumo, N. *J. Automot. Eng. (Part D Proc. Inst. Mech. Eng.)* **1993**, *207*, 23.

(2) Held, W.; Konig, A.; Richter, T.; Puppe, L. *Soc. Aut. Eng.* **1990**, paper 900496.

(3) Takeshima, S. U.S. Patent 5,017,538 May 21 **1991**.

(4) Kintachi, Y.; Hamada, H.; Tabat, M.; Sasaki, M.; Ito, T. *Catal. Lett.* **1990**, *6*, 239.

(5) Shin, S.; Hatakeyama, Y.; Ogawa, K.; Shimomura, K. *Mater. Res. Bull.* **1979**, *14*, 133.

(6) Shimokawabe, M.; Ohi, A.; Takesazawa, N. *React. Kinet. Catal. Lett.* **1994**, *52*, 393.

(7) Hwang, S. T.; Parravano, G. J. *Electrochem. Soc.* **1967**, *114*, 482.

(8) Leech, C. A.; Campbell, L. E. *Adv. Chem. Ser.* **1975** *143* 161.

(9) Shangguan, W. F.; Teraoka, Y.; Kagawa, S. *Appl. Catal. B* **1996**, *8*, 217.

(10) Panayotov, D.; Khristova, M.; Mehandjiev, D. *J. Catal.* **1995**, *156*, 219.

(11) Mehandjiev, D.; Panayotov, D.; Khristova, M. React. *Kinet. Catal. Lett.* **1986**, *33*, 273.

(12) Panayotov, D.; Mehandjiev, D.; Khristova, M. *Appl. Catal.* **1987**, *34*, 48.

(13) Clausen, B. S.; Grabaek, L.; Steffensen, G.; Hansen, P. L. *Catal. Lett.* **1993**, *20*, 23.

(14) Samant, M.G.; Bergeret, G.; Meitzner, G.; Gallezot, P.; Boudart, M. *J. Phys. Chem.* **1988**, *92*, 3542.

(15) Samant, M.G.; Bergeret, G.; Meitzner, G.; Gallezot, P.; Boudart, M. *J. Phys. Chem.* **1988**, *86*, 3547.

(16) Bazin, D.; Sayers, D.; Rehr, J. *J. Phys. Chem.* **1997**, *101*, 11040.

(17) Bazin, D.; Sayers, D.; Rehr, J.; Mottet, C. *J. Phys. Chem.* **1997**, *101*, 5332.

(18) Bellotto, M.; Rebours, B.; Clause, O.; Lynch, J.; Bazin, D.; Elkaim, E. *J. Phys. Chem.* **1996**, *100*, 8527.

(19) Bellotto, M.; Rebours, B.; Clause, O.; Lynch, J.; Bazin, D.; Elkaim, E. *J. Phys. Chem.* **1996**, *100*, 8535.

(20) Bazin, D.; Dexpert, H.; Lynch, J. *X-ray Absorption Fine Structure for catalysts and surfaces;* Iwasawa, Y., Ed.; World Scientific: Singapore, 1996.

(21) Michalowicz, A. *J. Phys. IV* **1997**, *C2−7* 235.

(22) Piquemal, J. Ph.; Leroy, C.; Michalowicz, A. Unpublished program available on the LURE web-site: www.lure.u-psud.fr, 1999.

(23) Revel, R.; Bazin, D.; Seigneurin, A.; Barthe, P.; Dubuisson, J. M.; Descamps, T.; Sonneville, H.; Poher, J. J.; Maire, F.; Lefrançois, P. *Nucl. Inst. Methods Phys. Res.* **1999**, *155*, 183.

(24) Warren, B. E. *X-ray Diffraction*; Addison-Wesley: Reading, MA, 1969.

(25) Cromer, D. T.; Mann, J. B. *Acta Crystallogr. A* **1968**, *24*, 321.

(26) Rodriguez-Carvajal, J *FULLPROF: A Program for Rietveld Refinement and Pattern Matching Analysis*; Abstracts of the Satellite Meeting on Powder Diffraction of the XV Congress of the IUCr, Toulouse, France 1990; p 127.

(27) Cerius Package. *Insight User guide*; M.S.I.: San Diego, 1995.

(28) Rehr, J. J.; Albers, R. C. *Phys. Rev. B* **1990**, *41*, 8149.

(29) Mustre, J.; Yacoby, Y.; Stern, E. A.; Rehr, J. J. *Phys. Rev. B* **1990**, *42*, 10843.

(30) Ankudinov, A. L.; Rehr, J. J. *Phys. Rev. B* **1997**, *56*, 1712.

(31) Coyler, L. M.; Greaves, G. N.; Carr, S. W.; Fox, K. K. *J. Phys. Chem.* **1997**, *101*, 10105.

(32) Newville, M.; Ravel, B.; Haskel, D.; Stern, E. A.; Yacoby, Y. *Physica B* **1995**, *208&209*, 154.

(33) See for documentation the FEFFIT web site: cars1.uchicago.edu:80/~newville/feffit/.

(34) Dobson, A. J. *An introduction to generalized linear models*; Chapman and Hall: London, 1990.

(35) Fernandez Colinas, J. M.; Otero Arean, C. *J. Solid. State Chem.* **1994**, *109*, 43.

(36) Lu, F. H.; Francke, P.; Nichols, C. S.; Diekmann, R. *J. Appl. Phys.* **1994**, *75* (2), 819.